Accuracy and stability in incompressible SPH (ISPH) based on the projection method and a new approach

Rui Xu *, Peter Stansby, Dominique Laurence

School of Mechanical, Aerospace, and Civil Engineering, University of Manchester, Sackville Street, Manchester M60 1QD, UK

A R T I C L E   I N F O

A B S T R A C T

The stability and accuracy of three methods which enforce either a divergence-free velocity field, density invariance, or their combination are tested here through the standard Taylor–Green and spin-down vortex problems. While various approaches to incompressible SPH (ISPH) have been proposed in the past decade, the present paper is restricted to the projection method for the pressure and velocity coupling. It is shown that the divergence-free ISPH method cannot maintain stability in certain situations although it is accurate before instability sets in. The density-invariant ISPH method is stable but inaccurate with random-noise like disturbances. The combined ISPH, combining advantages in divergence-free ISPH and density-invariant ISPH, can maintain accuracy and stability although at a higher computational cost. Redistribution of particles on a fixed uniform mesh is also shown to be effective but the attraction of a mesh-free method is lost. A new divergence-free ISPH approach is proposed here which maintains accuracy and stability while remaining mesh free without increasing computational cost by slightly shifting particles away from streamlines, although the necessary interpolation of hydrodynamic characteristics means the formulation ceases to be strictly conservative. This avoids the highly anisotropic particle spacing which eventually triggers instability. Importantly pressure fields are free from spurious oscillations, up to the highest Reynolds numbers tested.

1. Introduction

Smoothed Particle Hydrodynamics (SPH) is a fully Lagrangian method, where the fluid medium is discretized by interaction between particles rather than mesh cells. It was first introduced by Lucy [18], and Gingold and Monaghan [11]. The use of SPH has since widely expanded in numerous areas [20]. The basic concept of SPH is that continuous media are represented by discrete particles, whose movement prescribes the flow field. The particles have a kernel function to define their range of interaction, and the hydrodynamic variable fields are approximated by integral interpolations. Meshes are not needed in the simulation, which is a major advantage of SPH over Eulerian methods. SPH simulation of the incompressible flow is more challenging than the compressible case, and is a main research focus. The simulations of the incompressible flows can be achieved by two methods: (1) approximately simulating incompressible flows with a small compressibility, called Weakly Compressible SPH (WCSPH); (2) simulating flows by enforcing the incompressibility, called Incompressible SPH (ISPH). In ISPH methods the incompressibility has been generally achieved by the projection method [6,12,25,17]. The recent alternative approach of imposing the kinematic constraint of a constant volume for each fluid particle through non-thermodynamic pressure [8] is not considered in this paper. It is however potentially competitive as shown through comparisons with WCSPH in [8]. In this work, only the projection-based ISPH methods are studied.

---

* Corresponding author. Tel.: +44 161 306 2614.
  E-mail address: xuruihaixia@gmail.com (R. Xu).

WCSPH method has been most widely used in simulations of incompressible flows. However, with WCSPH, the pressure field strongly depends on a state equation, generally resulting in large pressure fluctuations. The accuracy can be improved by remeshing on a uniform grid, which is first introduced by Chaniotis et al. [3] in the context of SPH. But clearly this loses the mesh free characteristic. Moreover, to satisfy the Courant–Friedrichs–Lewy (CFL) time-step constraint, with a speed of sound in the CFL number expression, the time step is limited to a very small value. Compressibility also causes sound wave reflection at the boundaries. All these considerations make a fully incompressible algorithm a desirable alternative to couple pressure and velocity in SPH.

An approach for modelling incompressible flow with a free surface using a fully Lagrangian technique was proposed by Koshizuka et al. [14]. In this method, a penalty-like formulation was employed to adjust the pressure where density variations occurred. In 1998, Koshizuka et al. [15] presented another incompressible method. A pressure Poisson equation was solved instead of a penalty method with a source term proportional to density variation. In 1999, Cummins and Rudman [6] applied the projection method in SPH, which projects an intermediate velocity field onto a divergence-free field and a curl-free field respectively. Shao and Lo [25] used an incompressible method, similar to that in [15], to describe the free surface in dam-break flow. Colin et al. [5] proposed an improved Laplacian operator in a method similar to [6]. In 2007 and 2008, Lee et al. [16,17] pointed out that a truly ISPH method improved the accuracy of the SPH method. In 2007, different from the projection-based ISPH, the non-thermodynamic pressure is calculated in [8] to maintain the constant volume for each fluid particle. In 2007, Hu and Adams [12] proposed a stable algorithm to obtain both a velocity-divergence-free field and constant density, with an additional Poisson equation solution. In 2008, Fang and Parriaux [9] used a remeshing method to overcome the instability problem in the Lagrangian finite point method (LFPM). However, in the finite point method, strict conservation is not maintained.

In [12], it was pointed out that if only a divergence-free velocity field is enforced, density variation, or particle clustering could happen due to the spatial truncation error; moreover, this density error could accumulate during the simulation. But this problem is firstly addressed in [8] in a different context. Fang and Parriaux [9] stated that irregular particle distributions will exhibit increasing numerical errors in SPH, and for LFPM, an ill conditioned matrix in the linear system could appear. On the one hand, with the ISPH method proposed in [6,17], a divergence-free velocity field is enforced, but the particle spacing is not considered, which could introduce instability in the simulation, based on the study in [12,9]. On the other hand, in [25], the particle spacing can be well maintained, resulting from the enforcement of density invariance, but the divergence-free condition for velocity field is not enforced. To better illustrate the advantages and disadvantages of all these existing projection-based ISPH methods [6,25,12,17], they are applied and examined here, based on the open-source code SPHysics [26], recently extended to account for the incompressibility. Moreover, a new method, where the particle positions are shifted slightly across streamlines, and the hydrodynamic variables at new positions are interpolated by Taylor series, is presented here.

In this paper, the basic SPH methodology will be introduced in Section 2. The details about all the projection-based ISPH algorithms are introduced in Section 3. In Section 4, the finite volume commercial package STAR-CD is introduced. Three test cases, Taylor–Green vortices, vortex spin-down and lid-driven cavity, are simulated here and defined in Section 5. For the first two cases, Taylor–Green vortices and vortex spin-down, previous projection-based ISPH methods and a new approach providing stability and accuracy efficiently are applied. The latter is further demonstrated for lid-driven cavity simulations. The results and discussion are presented in Section 6.

2. SPH methodology

In the SPH method, the Navier–Stokes equations in Lagrangian form, shown below, are solved. The pressure gradient term and viscous term are approximated by the operators introduced later. Incompressibility here is enforced in the projection method by a pressure Poisson equation [4].

$$\nabla \cdot \mathbf{U} = 0 \tag{1}$$

$$\frac{d\mathbf{U}}{dt} = -\frac{1}{\rho}\nabla P + \nu\nabla^2\mathbf{U} + \mathbf{F} \tag{2}$$

2.1. Basic smoothed particle hydrodynamics (SPH) methodology

2.1.1. SPH interpolation

For a variable A, in SPH formalism, the value of A at a point $\mathbf{r}$ is written as a convolution product of the variable A with the Dirac δ function

$$A(\mathbf{r}) = \int A(\mathbf{r}')\delta(|\mathbf{r} - \mathbf{r}'|)d\mathbf{r}'. \tag{3}$$

In SPH, the δ function is approximated by a smoothing kernel function $\omega_h(|\mathbf{r} - \mathbf{r}'|)$, with a smoothing length h. Therefore, Eq. (3) can be approximated as

$$A(\mathbf{r}) \approx \int_{\Omega} A(\mathbf{r}')\omega_h(|\mathbf{r} - \mathbf{r}'|)d\mathbf{r}', \tag{4}$$

where Ω is the supporting domain. In a discretized format, the interpolation can be written as

$$A(\mathbf{r_i}) \approx \sum V_j A(\mathbf{r_j})\omega_h(r_{ij}). \tag{5}$$

where V_j is the volume of particle j. The particle density is given by

$$\rho(\mathbf{r}) \approx \sum m_j \omega_h(r_{ij}). \tag{6}$$

In the later parts, $\omega_h(r_{ij})$ will be briefly written as ω_{ij}.

In this paper, a fifth-order kernel [21] is used for all cases.

2.1.2. Gradient and divergence operator

The gradient operator for a general variable ϕ is given by

$$\nabla\phi_i \simeq -\sum_j V_j(\phi_i - \phi_j)\nabla\omega_{ij}. \tag{7}$$

One notable point is that the Einstein notation is not applied in this equation, and also the others below. The normalization [1,23] is applied to improve the accuracy. The expression for the kernel normalization can be read

$$\nabla\tilde{\omega}_{ij} = \mathbf{L}(\mathbf{r})\nabla\omega_{ij}. \tag{8}$$

where $\nabla\tilde{\omega}_{ij}$ is substituted into Eq. (7) for $\nabla\omega_{ij}$ as the normalized kernel first derivative, and

$$\mathbf{L}(\mathbf{r}) = \begin{pmatrix} \sum_j V_j(x_j - x)\frac{\partial\omega_{ij}}{\partial x} & \sum_j V_j(x_j - x)\frac{\partial\omega_{ij}}{\partial y} \\ \sum_j V_j(y_j - y)\frac{\partial\omega_{ij}}{\partial x} & \sum_j V_j(y_j - y)\frac{\partial\omega_{ij}}{\partial y} \end{pmatrix}^{-1}. \tag{9}$$

A similar operator with kernel normalization is used for the divergence calculation.

2.1.3. Viscous term and Laplacian operator

The viscous term expression applied in this paper is identical to the one suggested by Morris [21].

$$(\mu\Delta\mathbf{u})_i = \sum_j \frac{m_j(\mu_i + \mu_j)\mathbf{r}_{ij} \cdot \nabla\omega_{ij}}{\rho_j(r_{ij}^2 + \eta^2)}\mathbf{u}_{ij} \tag{10}$$

where m is the mass of the particle; ρ is the fluid density; μ is the dynamic viscosity; $\mathbf{u}_i$ is the velocity of particle i, $\mathbf{u}_{ij} = \mathbf{u}_i - \mathbf{u}_j$; $\mathbf{r}_i$ is the position of particle i, $\mathbf{r}_{ij} = \mathbf{r}_i - \mathbf{r}_j$; η is a small value to avoid singular denominator. An approximate Laplacian operator with the same format is used.

$$\Delta p_i = \sum_j 2\frac{m_j}{\rho_j}\frac{p_{ij}\mathbf{r}_{ij} \cdot \nabla\omega_{ij}}{(r_{ij}^2 + \eta^2)} \tag{11}$$

where $p_{ij} = p_i - p_j$. Other researchers [5,24] have proposed higher order operators, but these were not applied by [6,12,17,25] with whom we are making comparisons. Only Eq. (11) is used in this work. To maintain the viscous non-slip and homogeneous Neumann conditions for the wall, the mirror particle method [21] is used here.

2.2. The error caused by particle clustering

In [2,12,9], it was shown that increasingly irregular particle distributions will exhibit increasing numerical errors in results. Also, Fang and Parriaux [9] pointed out that an ill-conditioned matrix in the linear system could appear, with increasing non-uniformity of particle distribution. In this paper, the effect of particle clustering is an important theme.

In [19], Monaghan pointed out that the tensile instability in SPH will result in the clustering of particles. Fig. 1(a) shows the contour graph of the 2-D quintic kernel value, and Fig. 1(b) its first derivative. From the cross-section profile of the first derivative, at $x = 0$, Fig. 1(c), it can be seen that when particles are getting close to each other within a certain distance range, the interaction between them is not increased, but reduced. This non-physical behaviour of the kernel function will introduce error in simulations, such as in the pressure gradient, or the Laplacian operator, and cause the particle clustering phenomenon.

Although it is reported that the quadratic kernel can reduce this non-physical behaviour [7], its low-order accuracy and second derivative property, which strongly influences the stability of SPH method, limit its application in high-accuracy simulations. In [19], Monaghan introduced an extra artificial stress in the pressure term to overcome particle clustering problems. The effective alternative of remeshing on a uniform grid was first introduced by Chaniotis et al. [3] to remove clustering. In [12], the clustering problem is solved by introducing an extra internal iteration in the projection-based incom-
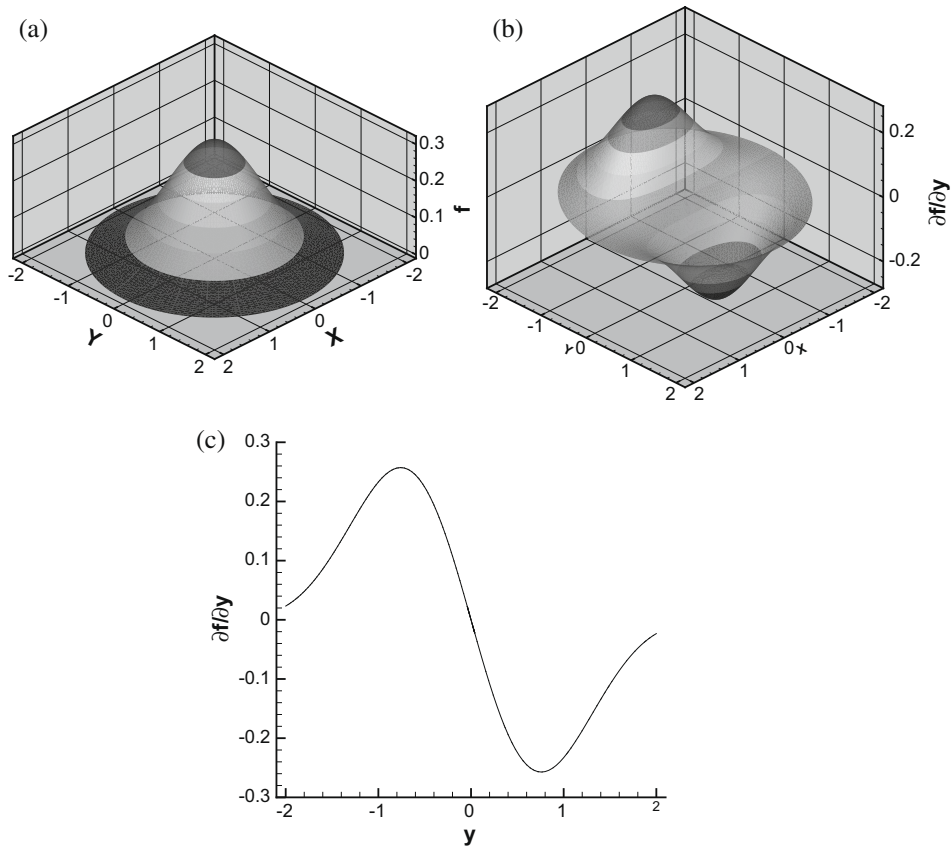
Fig. 1. (a) Contour graph for 2-D quintic kernel; (b) contour graph for the first derivative, $\frac{\partial f}{\partial y}$, of 2-D quintic kernel; (c) profile for the first derivative of quintic kernel, $\frac{\partial f}{\partial y}$, at cross-section $x = 0$.

pressible SPH algorithm to keep reasonable particle spacing. In this paper, a new method, based on projection method with slight particle shifting, is introduced to overcome particle clustering without relying on the background uniform mesh.

3. Projection-based incompressible SPH algorithm

3.1. ISPH based on keeping divergence-free velocity field (ISPH_DF) [6,17]

To keep a divergence-free velocity field, the projection method [4] is used, as first presented by Cummins and Rudman [6] in 1999. A second-order time marching scheme is applied, where both the density and mass of particles are constant. Particle positions, $\mathbf{r}_i^n$, are advected with velocity $\mathbf{u}_i^n$ to positions $\mathbf{r}_i^*$,

$$\mathbf{r}_i^* = \mathbf{r}_i^n + \Delta t \mathbf{u}_i^n. \tag{12}$$

An intermediate velocity $\mathbf{u}_i^*$ is calculated at the position, $\mathbf{r}_i^*$, based on the momentum equation without the pressure gradient term,

$$\mathbf{u}_i^* = \mathbf{u}_i^n + \left(\nu \nabla^2 \mathbf{u}_i^n + \mathbf{F}_i^n \right) \Delta t, \tag{13}$$

where $\mathbf{F}_i^n$ is the body force.

Solving the pressure Poisson equation (PPE) Eq. (14), the pressure at time $n + 1$ can be obtained from

$$\nabla \cdot \left(\frac{1}{\rho} \nabla p^{n+1} \right)_i = \frac{1}{\Delta t} \nabla \cdot \mathbf{u}_i^*. \tag{14}$$

The velocity at time $n + 1$, $\mathbf{u}_i^{n+1}$ will result from the projection of $\mathbf{u}_i^*$. Therefore,

$$\mathbf{u}_i^{n+1} = \mathbf{u}_i^* - \frac{\Delta t}{\rho} \nabla p_i^{n+1}. \tag{15}$$

The particle position is finally advanced in time,

$$\mathbf{r}_i^{n+1} = \mathbf{r}_i^n + \Delta t\left(\frac{\mathbf{u}_i^{n+1} + \mathbf{u}_i^n}{2}\right). \tag{16}$$

In an alternative formulation, Lee et al. [17] derived the velocity from the pressure correction with the particles at $\mathbf{r}_i^n$ before advancing their positions with the total velocity, termed truly incompressible SPH. This formulation was also applied here and produced results identical to [6] for the test cases investigated. This incompressible divergence-free SPH method will be referred to as ISPH_DF.

3.2. ISPH based on keeping density invariance (ISPH_DI) [25]

Similar to the method in [15], Shao and Lo [25] proposed a projection-based incompressible method to impose density invariance to describe free surface flows. An intermediate velocity, $\mathbf{u}_i^*$, is calculated without the pressure gradient term as before,

$$\mathbf{u}_i^* = \mathbf{u}_i^n + \left(\nu\nabla^2\mathbf{u}_i^n + \mathbf{F}_i^n\right)\Delta t. \tag{17}$$

The particles are convected to an intermediate position, $\mathbf{r}_i^*$,

$$\mathbf{r}_i^* = \mathbf{r}_i^n + \Delta t\mathbf{u}_i^*. \tag{18}$$

At this intermediate position, the intermediate velocity is projected on to two spaces, ∇P^{n+1} and $\mathbf{u}_i^{n+1}$, which is similar to ISPH_DF. But instead of calculating the pressure field P^{n+1} through a Poisson equation with a velocity divergence on the right hand side (RHS), the pressure field is obtained by solving a Poisson equation with a relative density difference on RHS, as shown in Eq. (19).

$$\nabla \cdot \left(\frac{1}{\rho^*}\nabla P^{n+1}\right) = \frac{\rho_0 - \rho^*}{\rho_0\Delta t^2} \tag{19}$$

And the intermediate velocity field will be corrected by the pressure gradient,

$$\mathbf{u}_i^{n+1} = \mathbf{u}_i^n - \frac{\Delta t}{\rho^*}\nabla P^{n+1}. \tag{20}$$

To complete the time step, as for ISPH_DF, a second-order time marching scheme is used.

$$\mathbf{r}_i^{n+1} = \mathbf{r}_i^n + \Delta t\left(\frac{\mathbf{u}_i^{n+1} + \mathbf{u}_i^n}{2}\right) \tag{21}$$

Eqs. (19) and (14) are actually equivalent, if one assumes the continuity equation for the incompressible flow to be valid at the intermediate position, $\mathbf{r}_i^*$, with

$$(\nabla \cdot \mathbf{u})_{\mathbf{r}_i^*} = -\left(\frac{1}{\rho}\frac{d\rho}{dt}\right)_{\mathbf{r}_i^*}. \tag{22}$$

Substituting Eq. (22) into Eq. (14), Eq. (19) can be obtained. The numerical performance of two Poisson equations, Eqs. (14) and (19), are quite different. In this work it is found that with Eq. (19) simulations are more stable, but the accuracy of ISPH has been deteriorated. This density-invariant ISPH method will be referred to as ISPH_DI.

3.3. ISPH based on combining both a divergence-free velocity field and a density-invariant field (ISPH_DFDI) [12]

In [12], Hu and Adams point out that if only a divergence-free velocity field is enforced, a large density variation will appear. They suggested that a divergence-free and density-invariance algorithm should be applied. This requires two pressure Poisson equations to be solved in this algorithm.

Similar to Shao and Lo's method [25], to keep the density constant, represented as $\rho_i^n = \rho_i^0$, the particle positions are adjusted. First, intermediate velocities and particle positions are obtained by

$$\mathbf{u}_i^{*,n+1/2} = \mathbf{u}_i^n + \left(\nu\nabla^2\mathbf{u}_i^n + \mathbf{F}_i^n\right)\frac{\Delta t}{2} \tag{23}$$

$$\mathbf{r}_i^{*,n+1} = \mathbf{r}_i^n + \mathbf{u}_i^{*,n+1/2}\Delta t \tag{24}$$

The intermediate particle density $\rho^{*,n+1}$ is calculated. And a Poisson equation

$$\frac{\Delta t^2}{2}\nabla \cdot \left(\left(\frac{1}{\rho}\nabla p\right)_i^n\right) = \frac{\rho_i^n - \rho_i^{*,n+1}}{\rho_i^n} \tag{25}$$

is solved to adjust particle position, shown later. If we define

$$\sigma_i = \sum_j \omega_{ij} \tag{26}$$

then

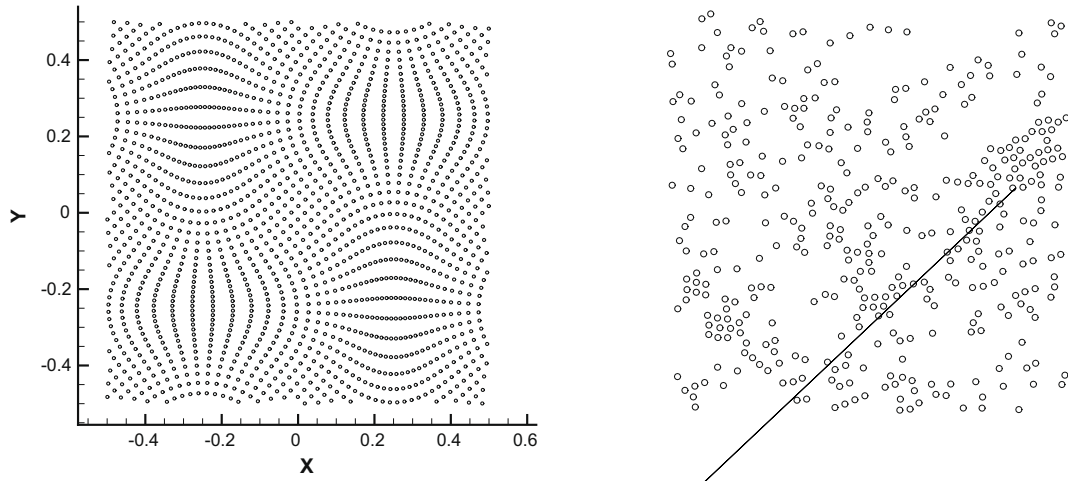$$\rho_i = \sum_j m_j \omega_{ij} = m_i \sigma_i. \tag{27}$$

With the relation $\rho_i^n = \rho_i^0 = m_i \sigma_i^0$ and $\rho_i^{*,n+1} = m_i \sigma_i^{*,n+1}$, Eq. (25) can be written as

$$\frac{\Delta t^2}{2} \nabla \cdot \left(\left(\frac{1}{\rho} \nabla p \right)_i^n \right) = \frac{\sigma_i^0 - \sigma_i^{*,n+1}}{\sigma_i^0}. \tag{28}$$

After the pressure is calculated, the particle positions are adjusted through the pressure gradient $(\frac{1}{\rho}\nabla p)_i^n$ following

$$\mathbf{r}_i^{n+1} = \mathbf{r}_i^{*,n+1} - \left(\frac{1}{\rho} \nabla p \right)_i^n \frac{\Delta t^2}{2} \tag{29}$$

During the simulation, the particle density will be recalculated at position $\mathbf{r}^{n+1}$ from Eq. (27). A certain criterion for the relative density difference, typically 1%, is set. If the criterion is not fulfilled, the particle positions will be adjusted by the following internal iteration.

$$\frac{\Delta t^2}{2} \nabla \cdot \left(\left(\frac{1}{\rho}\nabla p\right)_i^{n,m}\right) = \frac{\sigma_i^0 - \sigma_{i*}^{n+1,m}}{\sigma_i^0} \rightarrow \left(\frac{1}{\rho}\nabla p\right)_i^{n,m}$$

$$\mathbf{r}_i^{n+1,m+1} = \mathbf{r}_i^{n+1,m} - \left(\frac{1}{\rho}\nabla p\right)_i^{n,m}\frac{\Delta t^2}{2}$$

$$\sigma_{i*}^{n+1,m+1} \leftarrow \mathbf{r}_i^{n+1,m+1}$$

(30)

where m is the number of internal iterations.

As for ISPH_DF, a Poisson equation needs to be solved to keep the velocity field divergence-free. First, the velocity field is explicitly calculated without considering the pressure gradient term.

$$\mathbf{u}_i^{*,n+1} = \mathbf{u}_i^{*,n+1/2} + \left(v\nabla^2\mathbf{u}_i^{*,n+1/2} + \mathbf{F}_i^{*,n+1/2}\right)\frac{\Delta t}{2}$$

(31)

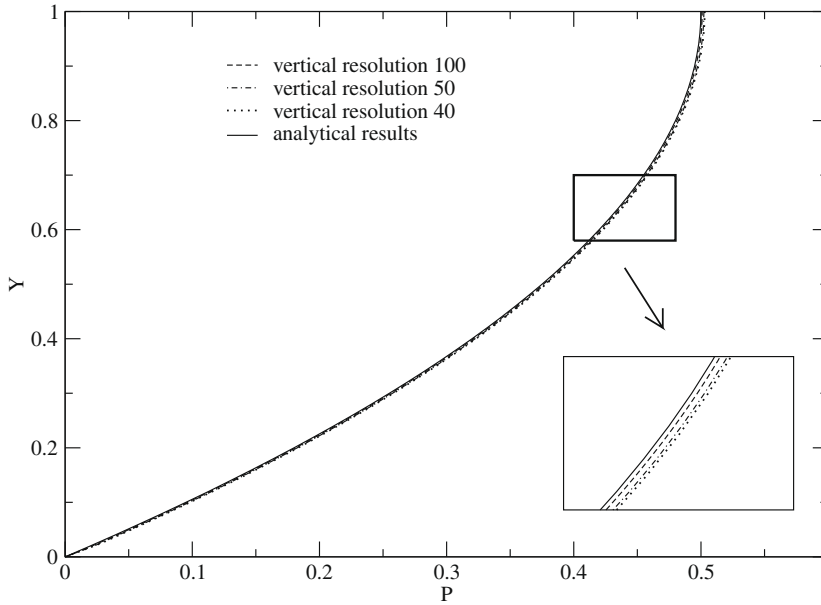The velocity field is then corrected by the pressure gradient,
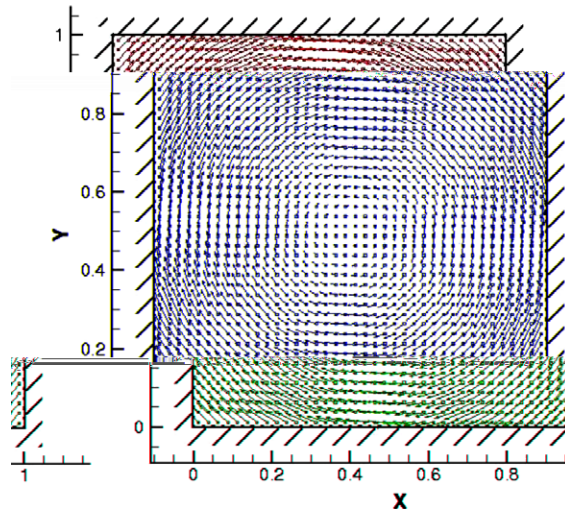

Fig. 4. Linear solver and boundary conditions test.

Fig. 5. The geometry and initial velocity field of vortex spin-down case.

$$\mathbf{u}_i^{n+1} = \mathbf{u}_i^{*,n+1} - \frac{\Delta t}{2\rho}\nabla p_i^{n+1} \tag{32}$$

where, the pressure field is obtained from the pressure Poisson equation.

$$\nabla \cdot \left(\frac{1}{\rho}\nabla p^{n+1}\right)_i = \frac{2}{\Delta t}\nabla \cdot \mathbf{u}_i^{*,n+1} \tag{33}$$

Similar to Eq. (19) in ISPH_DI, Eq. (25) or (28) is solved to prevent particle clustering, while Eq. (33) is used to keep a divergence-free velocity field. Uniform particle spacing improves the stability of simulations, as will be shown later. Through solving two Poisson equations, Eqs. (25) and (33), both the density invariance and divergence-free velocity field are approximated. This combined incompressible SPH method will be referred to as ISPH_DFDI.

3.4. ISPH_DF with shifting particle position (ISPH_DFS)

In ISPH_DF, particles move along the streamlines when the Lagrangian-form Navier–Stokes equations are solved accurately. The stretching and compressing of particle spacing, similar to the mesh distortion in the finite volume (FV) method,
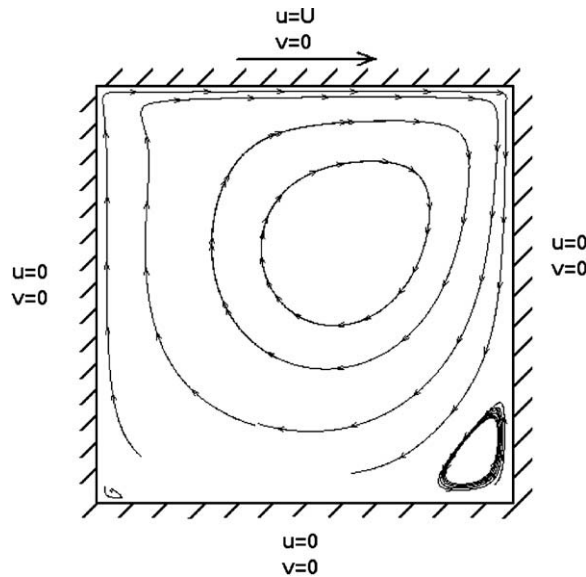

Fig. 6. Geometry of lid-driven cavity case. The graph shows the streamline in the case with $Re = 400$, simulated by ISPH_DFS, with a resolution of 60×60.
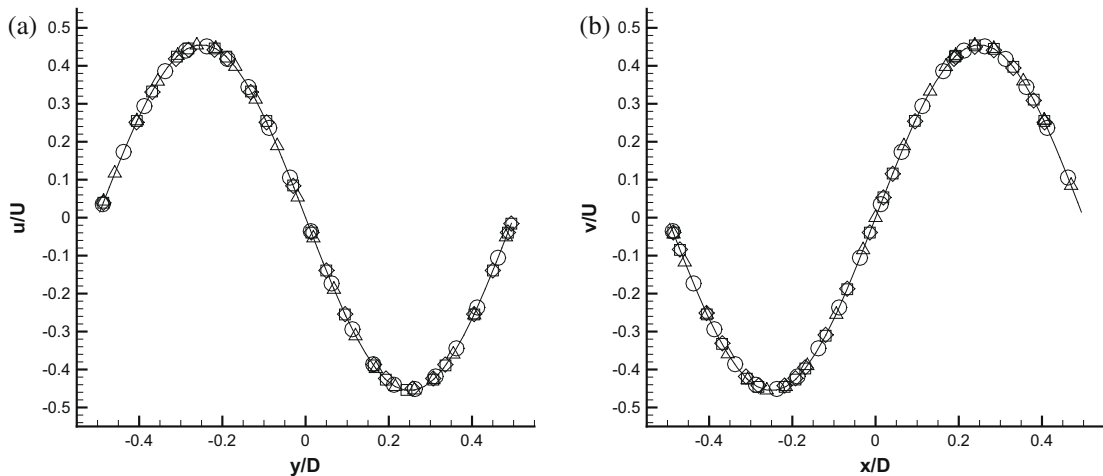

Fig. 7. Normalized velocity profiles in Taylor–Green vortices, $Re = 10, t = 0.1$ s, with a resolution of 40×40. Velocity components and distances are normalized with the velocity scale $U, U = 1$, and the square length $D, D = 1$. (a) Horizontal velocity component profile, at $x = 0.0$ m; (b) vertical velocity component profile, at $y = 0.0$ m. $\triangle$ = ISPH_DFDI; $\bigcirc$ = ISPH_DF; $\square$ = ISPH_DI; $\diamondsuit$ = ISPH_DFS; — = analytical results.

happen under certain conditions, such as Taylor–Green vortices shown in Fig. 2(a). It is observed in the simulations that this non-uniform particle distribution will hinder the convergence of linear solvers. Also, on the one hand, if the streamlines direct the particles towards each other, taking Taylor–Green vortices as an example, Fig. 3, the particles will cluster; on the other hand, the non-physical behaviour of the kernel, introduced in Section 2.2, will weaken the interaction between particles when particle distances are within a close range. Then particles will continue clustering if the inertial motion, determined by Re number, is strong enough. The error, caused by this kernel flaw, also causes the instability in the projection-based ISPH.

The following method stabilizes the accurate ISPH_DF method. The particle distribution is effectively well maintained, shown in Fig. 2(b). The pressure field is calculated as in ISPH_DF. And the particles are advanced, shifted slightly, and accordingly, the hydrodynamic variables are corrected by the Taylor series,

$$\phi_{i'} = \phi_i + \delta \mathbf{r}_{ii'} \cdot (\nabla \phi)_i + \mathcal{O}(\delta r_{ii'}^2) \tag{34}$$

where ϕ is a general variable; i and i' are the particle's old position and its new position respectively; $\delta \mathbf{r}_{ii'}$ is the distance vector between the particle's new position and its old position. In the following tests, only the first two terms are used in simulations, giving an order consistent with the Laplacian operator. Higher order accuracy may be achieved by extending
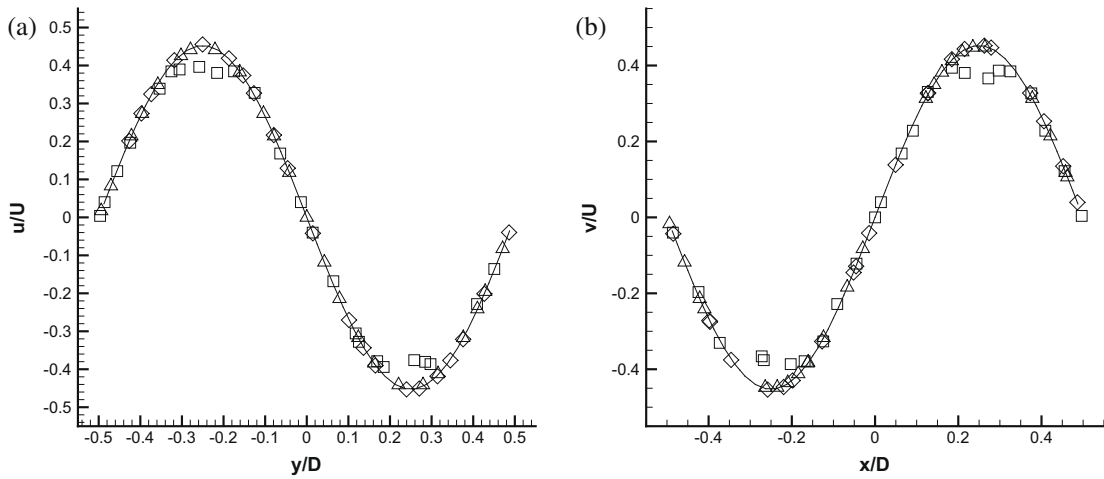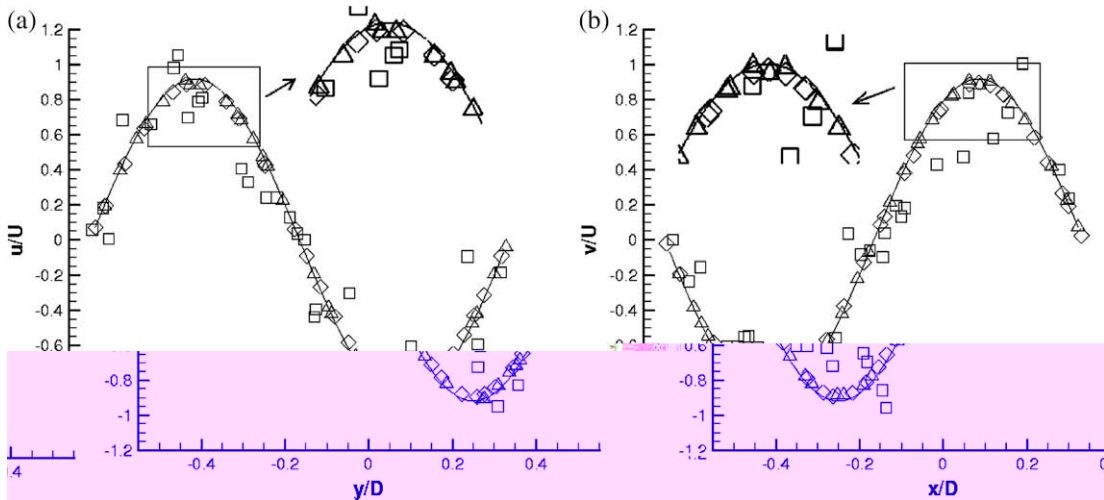

Fig. 8. Normalized velocity profiles in Taylor–Green vortices, $Re = 100, t = 1.0$ s, with a resolution of 40×40. Velocity components and distances are normalized with the velocity scale $U, U = 1$, and the square length $D, D = 1$. (a) Horizontal velocity component profile, at $x = 0.0$ m; (b) vertical velocity component profile, at $y = 0.0$ m. $\triangle$ = ISPH_DFDI; $\square$ = ISPH_DI; $\diamond$ = ISPH_DFS; — = analytical results.

Fig. 9. Normalized velocity profiles in Taylor–Green vortices, $Re = 1000, t = 1.0$ s, with a resolution of 40×40. Velocity components and distances are normalized with the velocity scale $U, U = 1$, and the square length $D, D = 1$. (a) Horizontal velocity component profile, at $x = 0.0$ m; (b) vertical velocity component profile, at $y = 0.0$ m. $\triangle$ = ISPH_DFDI; $\square$ = ISPH_DI; $\diamond$ = ISPH_DFS; — = analytical results.

the Taylor series and the divergence-free condition would be maintained with the same order as the interpolation.With the position shifting and interpolation, the particles redistribute themselves in a more isotropic manner, avoiding particle clustering in the direction of maximum compression and sparse discretisation error in the stretching direction. The method with particle shifting is called ISPH_DFS.

The idea of shifting particle positions has been proposed previously in the context of the Finite Volume Particle Method (FVPM) by Nestor et al. [22]. This allows the use of particle velocities with a correction, $\mathbf{u}'$, added to conserve fluid momentum. Different from FVPM, the adjustment of particle velocity here will introduce extra diffusion terms to the total momentum. The position shift is applied to particles, and the use of a first-order Taylor series interpolates hydrodynamic variable values at the new position, as given in Eq. (34). Similar to the velocity correction equation, $\mathbf{u}'$, in [22], but modifying the particle shifting magnitude, α, in relation to the particle convection distance and the particle size, the position shift reads

$$\delta \mathbf{r}_i = C \alpha \mathbf{R}_i \tag{35}$$

where C is a constant, set as 0.01–0.1, as discussed below; α is the shifting magnitude which is equal to the maximum particle convection distance $U_{max}dt$, with U_{max} the maximum particle velocity, and dt the time step; $\mathbf{R}_i$ is the shifting vector, and reads:
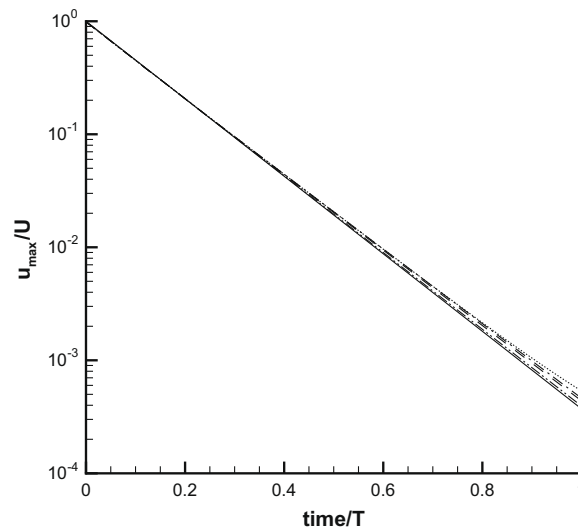

Fig. 10. Maximum velocity, u_{max}, decaying against time in Taylor–Green vortices, $Re = 10$, with a resolution of 40×40. Maximum velocity, u_{max}, is normalized with velocity scale U; time is scaled by T, where $T = D/U$. --- = ISPH_DF; ---- = ISPH_DI; ⋯ = ISPH_DFDI; --⋅-- = ISPH_DFS; — = analytical results.
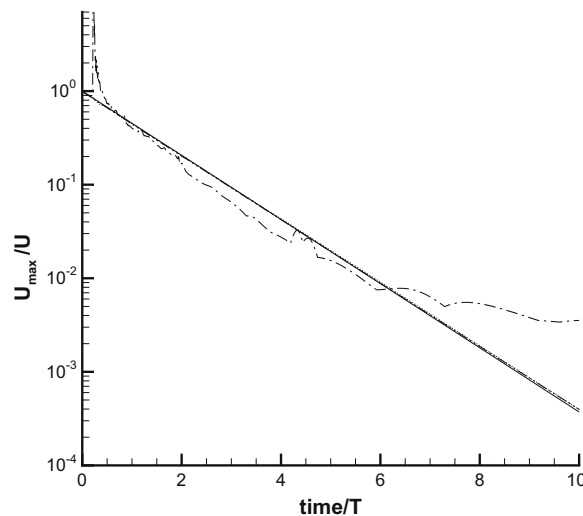

Fig. 11. Maximum velocity, u_{max}, decaying against time in Taylor–Green vortices, $Re = 100$, with a resolution of 40×40. Maximum velocity, u_{max}, is normalized with velocity scale U; time is scaled by T, where $T = D/U$. --⋅-- = ISPH_DI; ⋯ = ISPH_DFDI; --⋅-- = ISPH_DFS; — = analytical results.

$$\mathbf{R}_i = \sum_{j=1}^{M_i} \frac{\bar{r}_i^2}{r_{ij}^2} \mathbf{n}_{ij} \qquad (36)$$

where M_i is the number of neighbouring particles around particle i; r_{ij} is the distance between particle i and particle j; $\bar{r}_i$ is the average particle spacing in the neighbourhood of i, and

$$\bar{r}_i = \frac{1}{M_i} \sum_{j=1}^{M_i} r_{ij}; \qquad (37)$$

$\mathbf{n}_{ij}$ is the unit distance vector between particles i and j. The summation of $\mathbf{n}_{ij}$ actually represents the anisotropy of the particle spacings. $\bar{r}_i^2/r_{ij}^2$ is used here as a weighting function to reduce the influence from remote neighbouring particles. R_i is evaluated on a fixed particle map obtained after the evolution equation Eq. (16). No internal iteration for a converged particle position is needed here.

The shifting distance should be large enough to prevent instability and small enough not to cause inaccuracy due to the Taylor series correction. Values of C within the range 0.01–0.1 satisfy these criteria for these test cases and dependence on
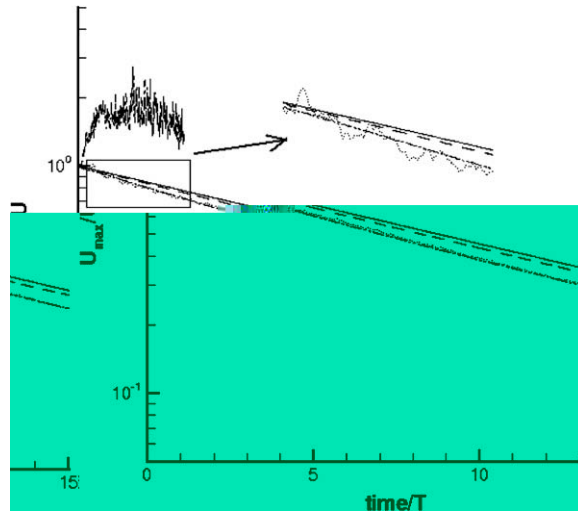

Fig. 12. Maximum velocity, u_{max}, decaying against time in Taylor–Green vortices, $Re = 1000$. Maximum velocity, u_{max}, is normalized with velocity scale U; time is scaled by T, where $T = D/U$. $-\cdot\cdot-$ = ISPH_DI (40×40); $\cdots$ = ISPH_DFDI (40×40); $-\cdot\cdot-$ = ISPH_DFS (40×40); $---$ = ISPH_DFS (80×80); $—$ = analytical results.
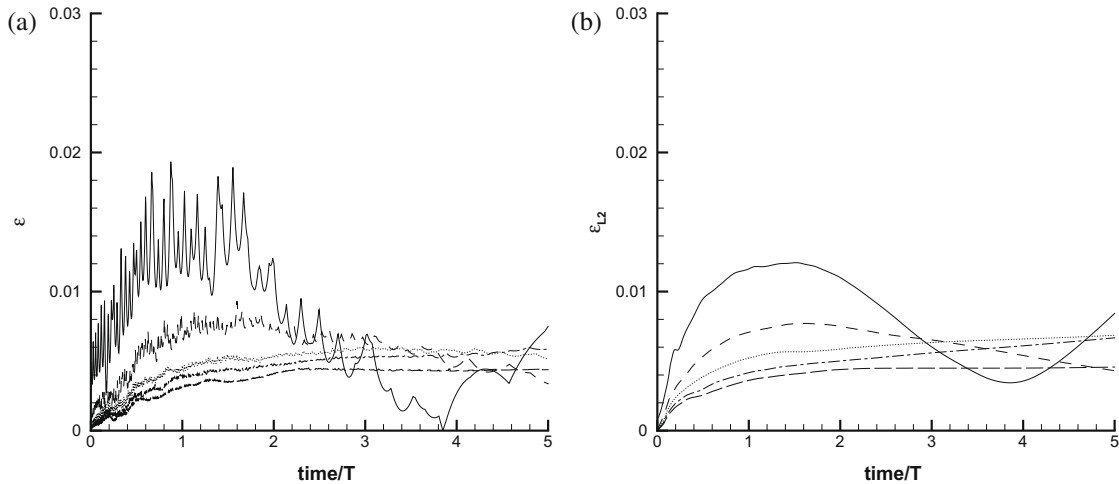

Fig. 13. Estimated relative error profiles for the horizontal velocity component, u, with different resolutions, $Re = 100$. (a) Estimated error based on Eq. (41); (b) estimated error based on L2 norm. The time is normalized by T, and $T = U/D$. $—$ = 40×40; $---$ = 80×80; $\cdots$ = 120×120; $-\cdot\cdot-$ = 160×160; $---$ = 200×200.

Reynolds number was not observed. A value of 0.04 is generally used. In [22], an average particle spacing, as defined in Eq. (37), is used as the shifting magnitude α, considering the influence of particle size. However, it is observed in simulations that when shifting distances are much larger than convection distances, large numerical error will appear in the fields of hydrodynamic variables, even with the Taylor-series updating. To avoid this an upper limit on shifting distance α is simply set as $U_{max}dt$, updated at each time step. Note also that the shifting distance is always much less than the smoothing length h.

All in all, the algorithm can be summarized here as

- Convect particle i to an intermediate position $\mathbf{r}_i^*$, as shown in Eq. (12);
- Calculate an intermediate velocity, $\mathbf{u}_i^*$, without the pressure gradient term, as shown in Eq. (13);
- Calculate the pressure from the Poisson equation, as shown in Eq. (14);
- Correct the intermediate velocity, $\mathbf{u}_i^*$, by the pressure gradient to obtain the velocity for next time step, $\mathbf{u}_i^{n+1}$, shown in Eq. (15);
- The particle position is centred in time, as shown in Eq. (16);
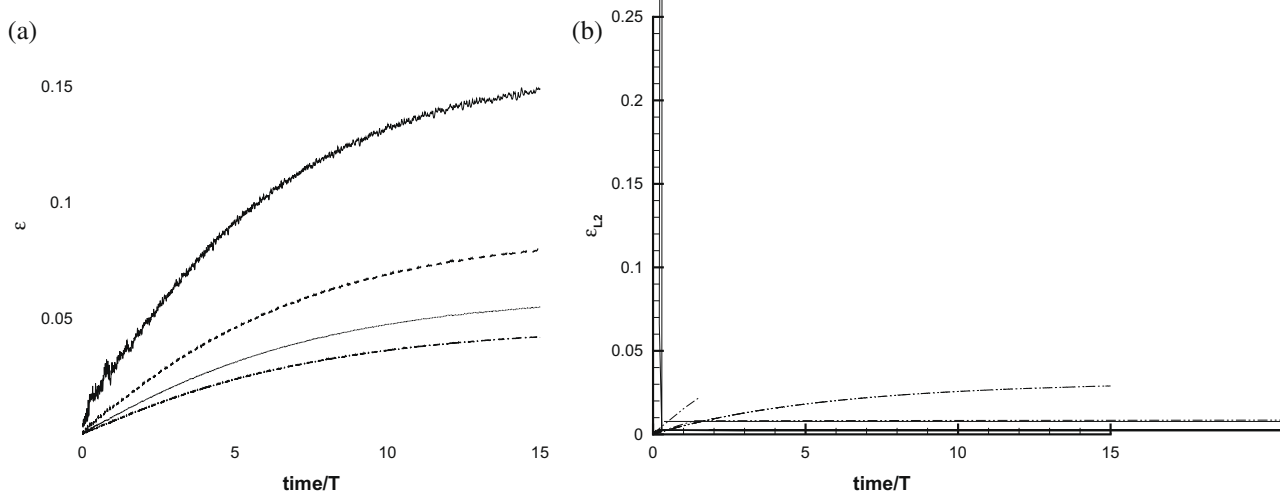- Shift the particle by Eq. (35);

Fig. 14. Estimated relative error profiles for the horizontal velocity component, u, with different resolutions, $Re = 1000$. (a) Estimated error based on Eq. (41); (b) estimated error based on L2 norm. The time is normalized by T, and $T = U/D$. — $= 40 \times 40$; - - - $= 80 \times 80$; $\cdots = 120 \times 120$; -·- $= 160 \times 160$; – – $= 200 \times 200$; -··- $= 240 \times 240$.
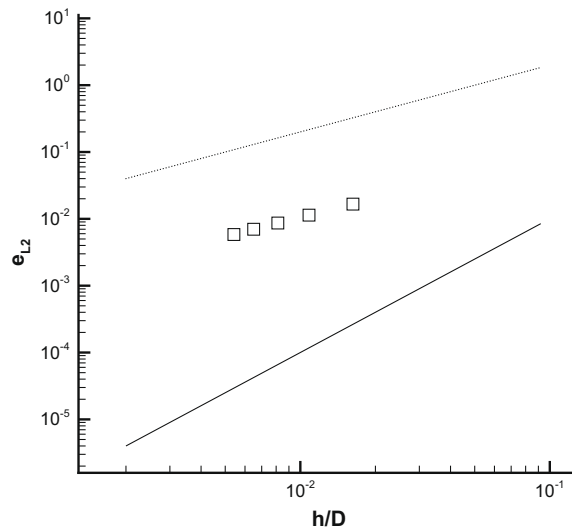

Fig. 15. Spatial accuracy estimation for the horizontal velocity component, u, with ISPH_DFS, $Re = 1000, t = 10.0$ s. The smoothing length, h, is normalized by the square length D, where $D = 1$. □ = the estimated simulation error, e_{l2}; $\cdots$ = slope of dr^1; — = slope of dr^2.

- Correct the velocity field by Eq. (34);
- Continue the calculation for next time step.

This method is actually similar in concept to the remeshing method in [3] using a fixed mesh but it maintains the meshless characteristic. The shifting of particle position and corresponding interpolation will introduce truncation errors in the results which will however be shown below to have negligible effect on the accuracy. This small change in ISPH_DF makes this method much more robust. And the efficiency of simulations is improved, comparing with ISPH_DFDI. It should be pointed out here that this method is not a strictly conservative method, similar to LFPM [9].

3.5. Linear solver

A Bi-Conjugate Gradients Stabilized solver (BiCGSTAB), with Jacobi preconditioner, is used to solve the linear system. A small calculation is conducted to test the linear solver and boundary conditions with mirror particles. A 1-D channel with periodic boundaries in x direction is set up. At the top of the channel, $y = 1$, a homogeneous Neumann boundary, $\frac{dP}{dy} = 0$, is set; at the bottom, $y = 0$, a Dirichlet boundary, $P = 0$, is set. The equation $\frac{d^2P}{dy^2} = -1$ is solved with different resolutions. The solver is tested with 40, 50 and 100 particles in the vertical direction, and compared with the analytical solution, $P = -0.5y^2 + y$, shown in Fig. 4. During all simulations, the convergence criterion is set as 1.0×10^{-5} for the normalized residual.

4. STAR-CD commercial package

Reference solutions for vortex spin-down and lid-driven cavity cases can probably be digitalized from the literature, but with cheap and fast convergence of commercial CFD codes on 2D cases, we simply computed these cases again on a fine Cartesian grid with the well-known STAR-CD, a Finite Volume commercial CFD code (see e.g. Jasak and Gosman [13] for a

Table 1
Computing costs comparison for Taylor–Green vortices with a resolution of 40×40. Physical time = 2.0 s. The same time step is used for all the methods under the same Reynolds situation.

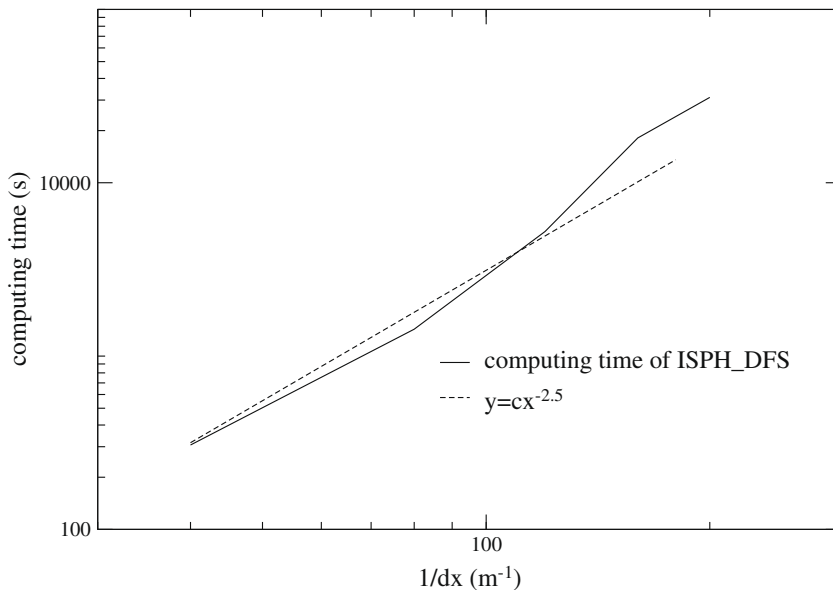|	$Re = 10$	$Re = 100$	$Re = 1000$
ISPH_DF	1,103 s	Unstable	Unstable
ISPH_DI	1,091 s	1,250 s	1,323 s
ISPH_DFDI	4,000 s	5,352 s	5,625 s
ISPH_DFS	1,213 s	1,281 s	1,387 s

Fig. 16. Computing cost of ISPH_DFS, for physical time 2.0 s on a Dell OPTIPLEX GX620 PC, with a Dual Core 3.2 GHz CPU and 2 GB memory, against the inverse particle spacing for Taylor–Green vortices, $Re = 1000$.

description and test of the FV algorithm). The convergence criterion is set as 10^{-5}. The PISO algorithm is used for pressure and velocity coupling. Second-order differencing schemes are used for convection terms in the calculation.

5. Simulation cases

5.1. Taylor–Green vortices

The Taylor–Green vortices simulations are conducted. The analytical velocity field is

$$
\begin{aligned}
u &= -Ue^{bt}\cos(2\pi x)\sin(2\pi y) \\
v &= Ue^{bt}\sin(2\pi x)\cos(2\pi y)
\end{aligned}
\tag{38}
$$

where U is the velocity scale, equal to 1.0 m/s here; kinematic viscosity v are 0.1 m^2/s,0.01 m^2/s and 0.001 m^2/s in three runs with three different Reynolds numbers, $Re = 10, Re = 100, Re = 1000; b = -\frac{8\pi^2}{Re}$ is the decay rate of the velocity field; u and v are the horizontal and vertical velocity components respectively. Different resolutions are used to investigate the spatial accuracy of ISPH_DFS. The Reynolds number is calculated by

$$
Re = \frac{UD}{v}
\tag{39}
$$

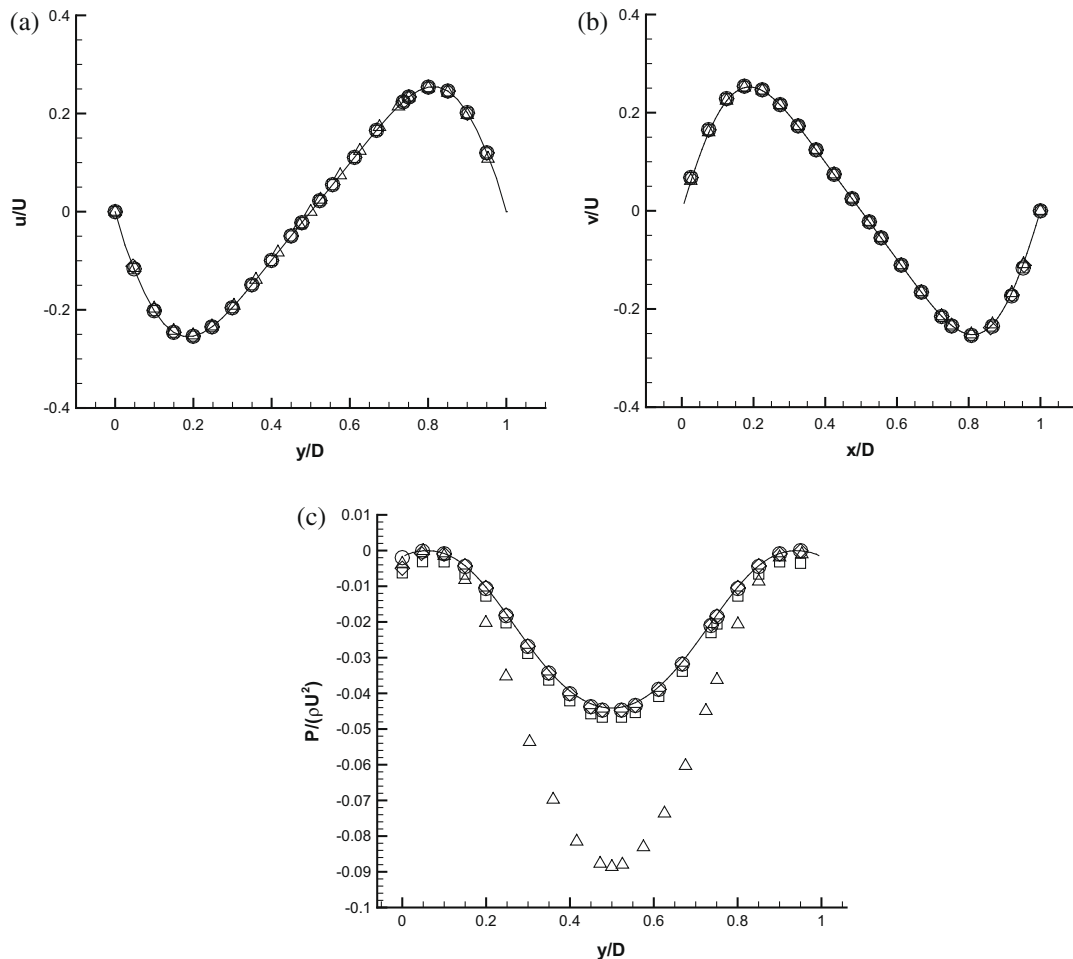where D is the length of the unit square side.

Fig. 17. Velocity and pressure profiles in vortex spin-down, $Re = 10, t = 0.1$ s, with a resolution of 40×40. Velocity components are normalized with the velocity scale $U, U = 1$; the coordinates are normalized with the square length $D, D = 1$; the pressure is normalized with ρU^2, where ρ is the fluid density. (a) Horizontal velocity component profile, at $x = 0.0m$; (b) vertical velocity component profile, at $y = 0.0$ m; (c) pressure profile at $x = 0.0$ m. $\triangle$ = ISPH_DFDI; $\bigcirc$ = ISPH_DF; $\square$ = ISPH_DI; $\diamond$ = ISPH_DFS; $-$ = STAR-CD.

Because of the existence of analytical results for Taylor–Green vortices, the accuracy of the algorithm and the code can be tested here. During simulations, it is observed that, under high Reynolds situations, the particle spacings are highly compressed in one direction, but stretched in the other roughly normal direction, with ISPH_DF. Because of the error caused by highly-distorted particle spacings, as mentioned before, the convergence with ISPH_DF can fail. For all values of Reynolds number, the four projection-based ISPH methods are applied. The accuracy, stability and computing expense of the four methods are compared.

5.2. Vortex spin-down

Similar to Taylor–Green vortices case, in vortex spin-down simulations, a vortex is bounded by four walls, placed in the middle of the domain, shown in Fig. 5. The vortex spin-down case is simulated for $Re = 10, Re = 100$ and $Re = 1000$. An initial velocity field is given by

$$
\begin{aligned}
u &= U(y - 0.5) \\
v &= U(0.5 - x)
\end{aligned}
\tag{40}
$$

in a unit square. 41×41 particles, equivalent to a resolution of 40×40 in the FV method, are used to compare four projection-based ISPH methods. The Reynolds number calculation is the same as that in Taylor–Green vortices, Eq. (39). Also, D, U and v are the same as those in Taylor–Green vortices.
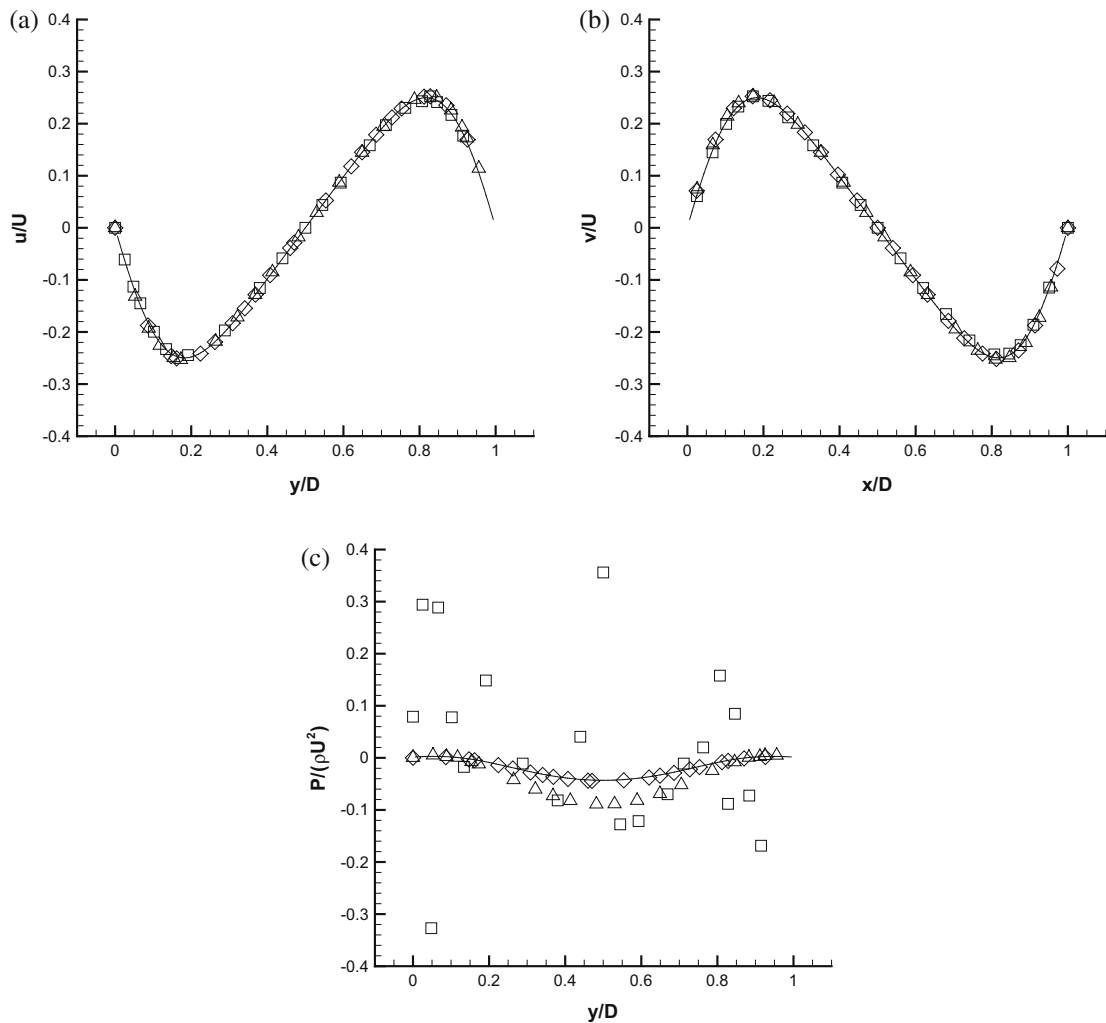

Fig. 18. Velocity and pressure profiles in vortex spin-down, $Re = 100, t = 1.0$ s, with a resolution of 40×40. Velocity components are normalized with the velocity scale $U, U = 1$; the coordinates are normalized with the square length $D, D = 1$; the pressure is normalized with ρU^2, where ρ is the fluid density. (a) Horizontal velocity component profile, at $x = 0.0$ m; (b) vertical velocity component profile, at $y = 0.0$ m; (c) pressure profile at $x = 0.0$ m. $\triangle$ = ISPH_DFDI; $\square$ = ISPH_DI; $\diamond$ = ISPH_DFS; $-$ = STAR-CD.

The accuracy, stability and computing time are compared among all the four projection-based ISPH methods. During simulations, it is found that particle spacings cannot be well maintained if ISPH_DF is used. It is the same as the findings in [9] that the irregular particle distribution hinders the convergence of the linear solver, and sometimes even causes the convergence to fail.

5.3. Lid-driven cavity

The lid-driven cavity problem has long been used a test or validation case for new codes or new solution methods. A good set of data for comparison is [10], where the data are listed out in a table for different Reynolds number situations. The two-dimensional geometry is shown in Fig. 6. In simulations, the fluid is accelerated by the lid at the top of the cavity to a steady state. Simulations with fully-developed flows are compared with data in [10] and STAR_CD results.

In this test case, only ISPH_DFS is used. The Reynolds number calculation is the same as that in Taylor–Green vortices. U and D are set to 1 m/s and 1 m for convenience. Reynolds numbers, $Re = 100, Re = 400$ and $Re = 1000$, are simulated.

6. Results and discussion

In this section, all simulations are run on a computer with a Dual Core 3.2 GHz CPU and 2 GB memory. Computing cost for different projection-based ISPH methods are compared in Taylor–Green vortices and vortex spin-down.
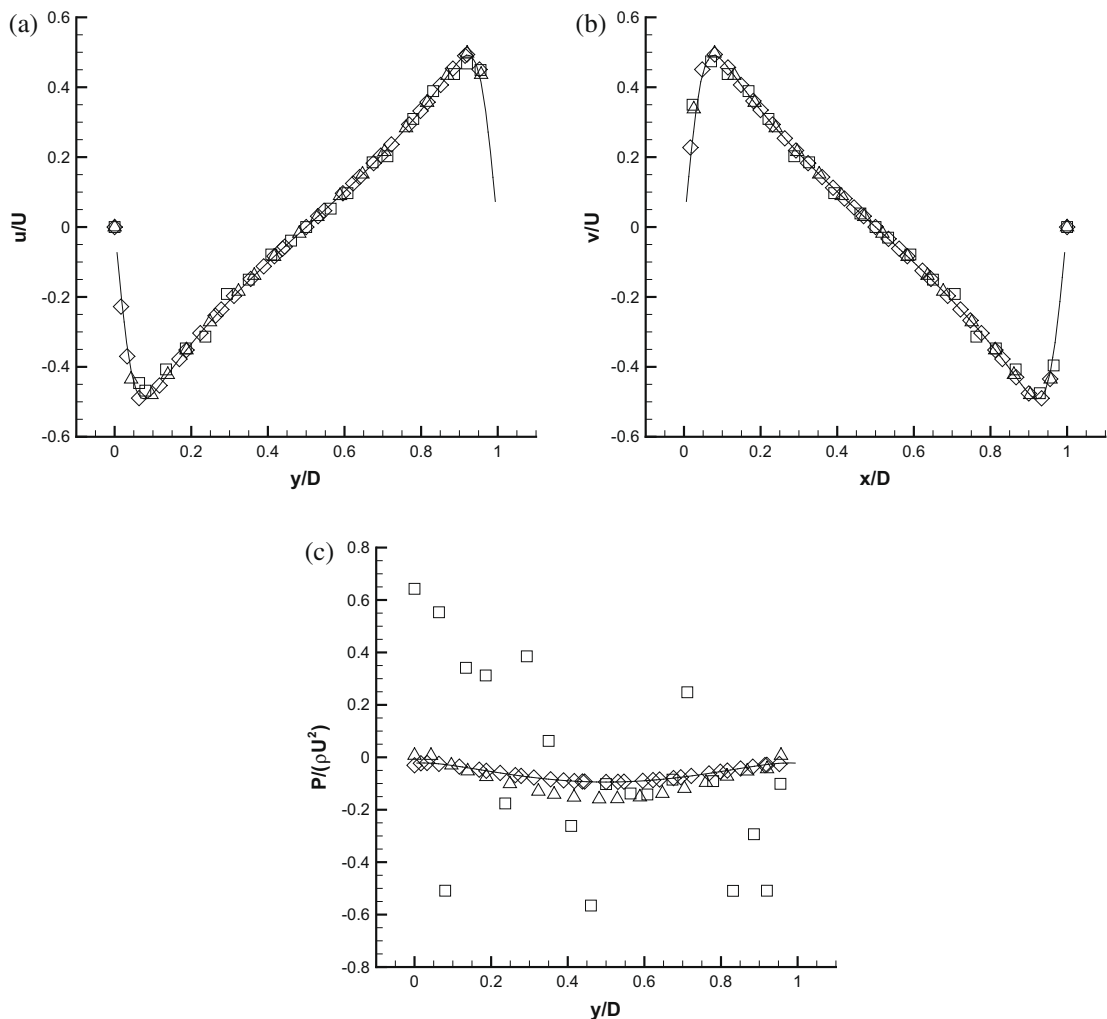

Fig. 19. Velocity and pressure profiles in vortex spin-down, $Re = 1000, t = 1.0s$, with a resolution of 40×40. Velocity components are normalized with the velocity scale $U, U = 1$; the coordinates are normalized with the square length $D, D = 1$; the pressure is normalized with ρU^2, where ρ is the fluid density. (a) Horizontal velocity component profile, at $x = 0.0$ m; (b) vertical velocity component profile, at $y = 0.0$ m; (c) pressure profile at $x = 0.0$ m. $\triangle$ = ISPH_DFDI; $\square$ = ISPH_DI; $\diamond$ = ISPH_DFS; — = STAR-CD.

6.1. Taylor–Green vortices results

Taylor–Green vortices are simulated in this work, with $Re = 10, Re = 100, Re = 1000$. Different resolutions are used with $Re = 100$ and $Re = 1000$ cases to investigate accuracy. For $Re = 10$, all four methods give stable and accurate solutions. However, when the Re number increases to 100, the particle spacings are compressed in one direction, and stretched in the other direction roughly normal, as shown in Fig. 2. When particles cluster together as happens at the four points (± 0.25 m, ± 0.25 m) in Fig. 3, the error caused by the kernel flaw, presented in Section 2.2, will increase with decrease in the particle spacing. The clustering cannot be avoided for high Reynolds situations if particles move accurately along streamlines. It is observed that this error will accumulate, and jeopardize the simulation stability for the higher Reynolds number situations.

Fig. 7 presents the normalized velocity component, u and v, profiles, at $x = 0.0$ m and $y = 0.0$ m, $t = 0.1$ s, with $Re = 10$; Figs. 8 and 9 at time $t = 1.0$ s, for $Re = 100$ and $Re = 1000$ cases respectively. It can be observed in Fig. 7 that all four projection-based ISPH methods can provide very good prediction for the velocity field with $Re = 10$. When the Reynolds number increases to 100, ISPH_DF could not stably simulate the flow development, while the other three methods could continue
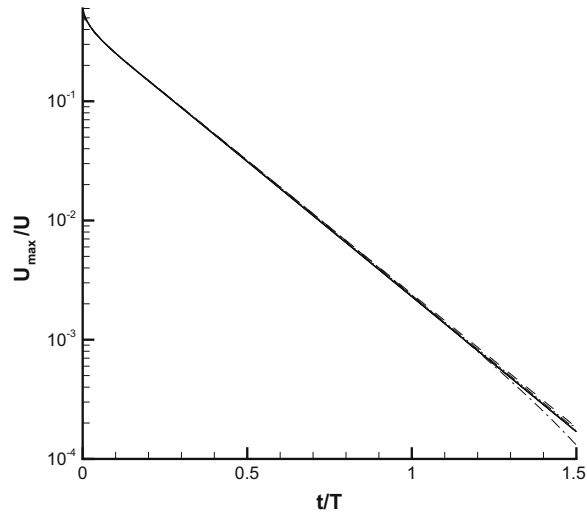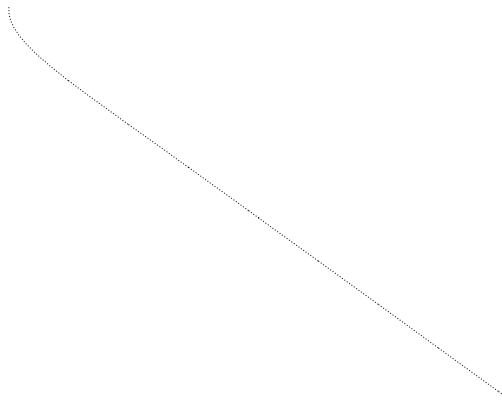

Fig. 20. Maximum velocity magnitude, U_{max}, decaying against time in vortex spin-down, $Re = 10$, with a resolution of 40×40. Maximum velocity, U_{max}, is normalized with velocity scale U; the physical time, t, is normalized with T, where $T = U/D$. --- = ISPH_DF; –·– = ISPH_DI; ··· = ISPH_DFDI; –··– = ISPH_DFS; — = STAR-CD.

simulations. In Fig. 8, it is shown that ISPH_DFDI and ISPH_DFS predict the velocity field accurately; ISPH_DI underpredicts the velocities at $x = \pm 0.25$ m and $y = \pm 0.25$ m. Increasing Reynolds number to 1000, ISPH_DFS provides smooth velocity profiles, but slightly underpredicts magnitudes; with ISPH_DI method, substantial numerical noise is generated; with ISPH_DFDI, some small numerical noise occurs at $y = \pm 0.25$ m and $x = \pm 0.25$ m, shown in enlarged parts of profiles in Fig. 9.
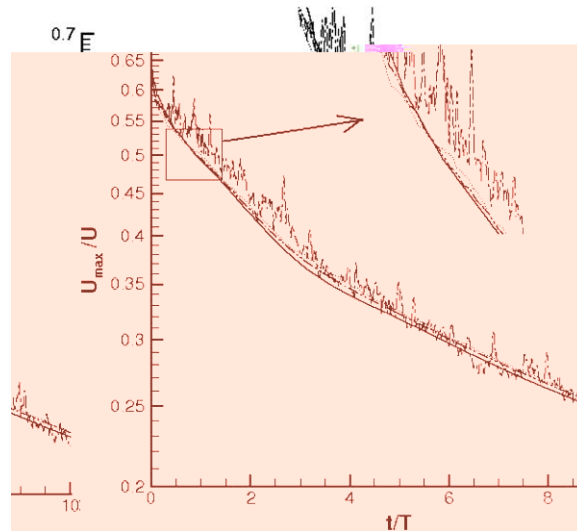

Fig. 22. Maximum velocity magnitude, U_{max}, decaying against time in vortex spin-down, $Re = 1000$, with a resolution of 40×40. Maximum velocity, U_{max}, is normalized with velocity scale U; the physical time, t, is normalized with T, where $T = U/D$. -·- = ISPH_DI; ··· = ISPH_DFDI; -··- = ISPH_DFS; — = STAR-CD.

Table 2
Computing costs comparison for vortex spin-down with a resolution of 40×40. Physical time $t = 2.0s$. The same time step is used for all the methods under the same Reynolds situation.

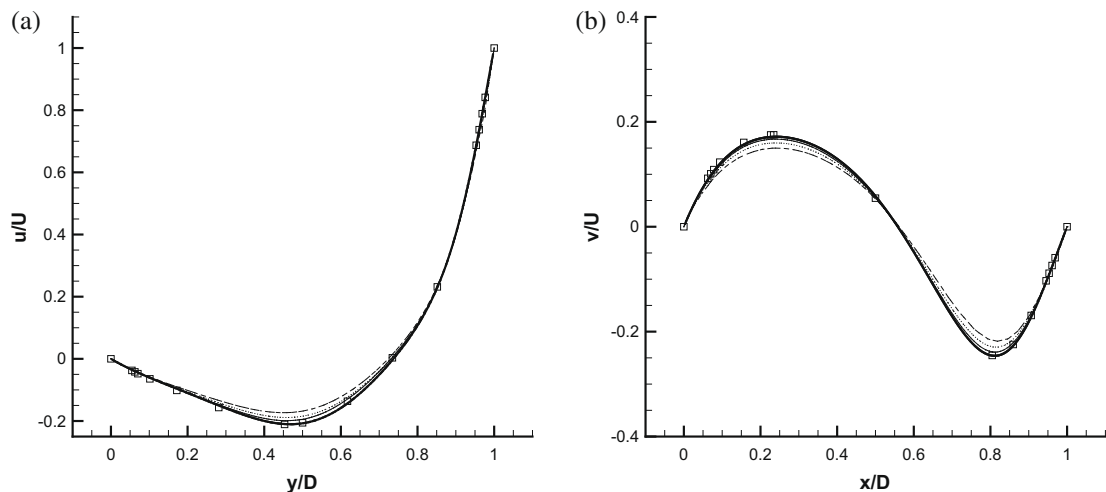|	$Re = 10$	$Re = 100$	$Re = 1000$
ISPH_DF	913 s	Unstable	Unstable
ISPH_DI	934 s	997 s	1,233 s
ISPH_DFDI	1262 s	5339 s	7679 s
ISPH_DFS	965 s	1067 s	1395 s

Fig. 23. Velocity profiles in lid-driven cavity, $Re = 100$. Velocity components are normalized with the lid velocity $U, U = 1$. The distances are normalized with the square length $D, D = 1$. (a) Horizontal velocity component profile, at $x = 0.0$ m; (b) vertical velocity component profile, at $y = 0.0$ m. --- = results with 41×41 resolution; ··· = results with 81×81 resolution; — = results with 161×161 resolution; Thick solid line = STAR-CD with 160×160 resolution; □ = Ghia 1982 [10].

Figs. 10–12 present the maximum velocity magnitude, u_{max}, decays against time for $Re = 10, Re = 100$ and $Re = 1000$, respectively. For the low Reynolds case, $Re = 10$, all the methods stably simulate the flow development, and ISPH_DFS gives the most accurate prediction, shown in Fig. 10. Increasing Reynolds number to, or over 100, only ISPH_DI, ISPH_DFDI and ISPH_DFS are presented, due to stability reasons. From Figs. 11 and 12, it can be seen that ISPH_DI does not provide accurate prediction. ISPH_DFDI could simulate the flow with $Re = 100$. But with $Re = 1000$, and the same particle resolution, 40×40, certain numerical noise appears on the profile at the beginning of the flow development, shown in the enlarged part in Fig. 12. Results with $Re = 1000$ were also not reported in [12]. Because ISPH_DFS underpredicts the maximum velocity magnitude, u_{max}, with a resolution of 40×40, a run with a higher resolution of 80×80 is conducted. Convergence towards analytical results is obtained.

To quantify the error in the ISPH_DFS methods, profiles of an estimated relative error are plotted out. In [12,3], a relative error, ε, is calculated, and defined as

$$\varepsilon = \left| \frac{\phi_{ex,max} - \phi_{ISPH,max}}{\phi_{ex,max}} \right|, \tag{41}$$
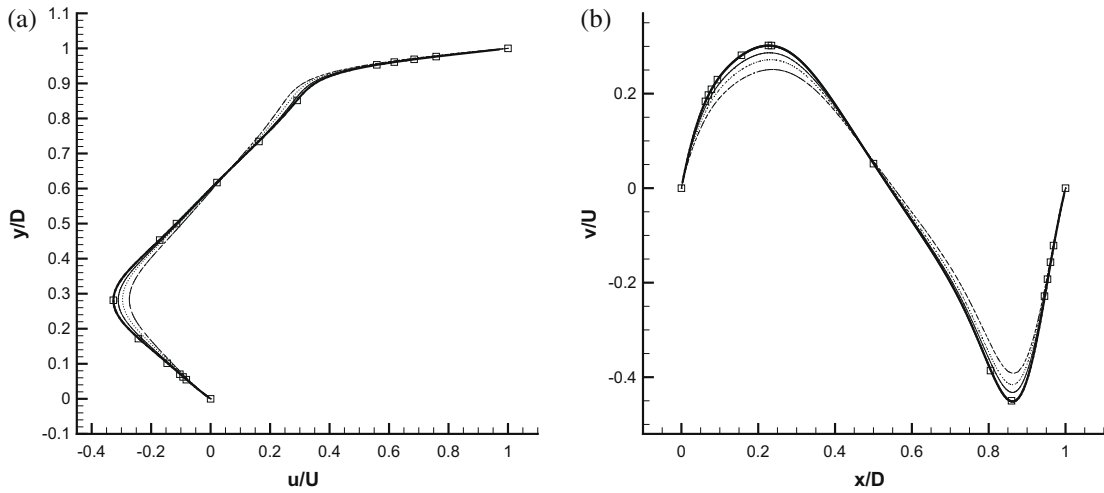

Fig. 24. Velocity profiles in lid-driven cavity, $Re = 400$. Velocity components are normalized with the lid velocity $U, U = 1$. The distances are normalized with the square length $D, D = 1$. (a) Horizontal velocity component profile, at $x = 0.0$ m; (b) vertical velocity component profile, at $y = 0.0$ m. – – – = results with 81×81 resolution; $\cdots$ = results with 161×161 resolution; — = results with 241×241 resolution; Thick solid line = STAR-CD with 160×160 resolution; $\square$ = Ghia 1982 [10].
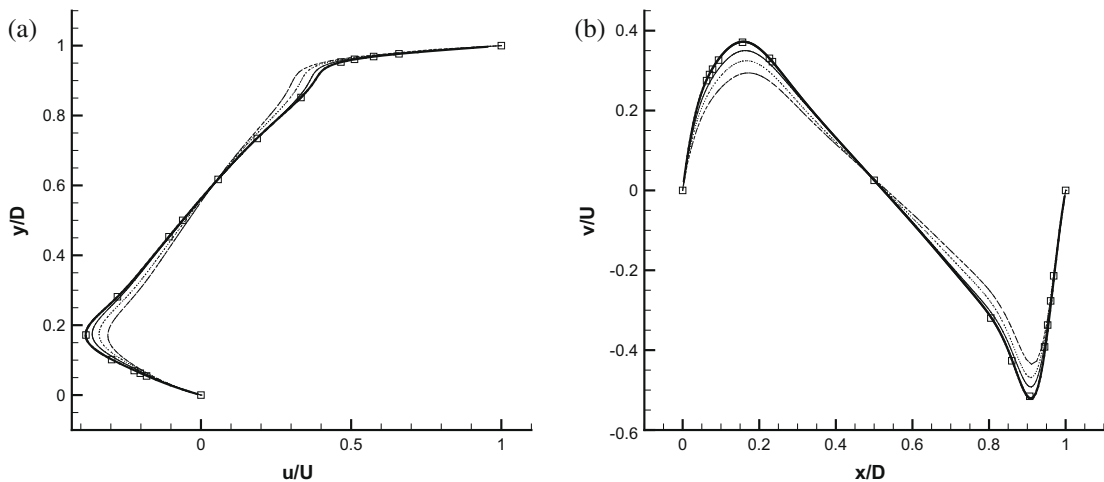

Fig. 25. Velocity profiles in lid-driven cavity, $Re = 1000$. Velocity components are normalized with the lid velocity $U, U = 1$. The distances are normalized with the square length $D, D = 1$. (a) Horizontal velocity component profile, at $x = 0.0$ m; (b) vertical velocity component profile, at $y = 0.0$ m. --- = results with 81×81 resolution; $\cdots$ = results with 161×161 resolution; — = results with 241×241 resolution; Thick solid line = STAR-CD with 160×160 resolution; $\square$ = Ghia 1982 [10].

where $\phi_{ex,max}$ and $\phi_{ISPH,max}$ are respectively the exact and simulated maximum values of a general variable, ϕ

was also obtained in [17]. We also tested redistribution of particles on a uniform mesh, following Chaniotis et al.[3], and very similar errors were obtained.

In Table 1, the computing costs for the four methods are listed. ISPH_DFDI is the most time-consuming method. The computing cost of ISPH_DFS method is only slightly more than ISPH_DF and ISPH_DI. As an example, the computing cost of ISPH_DFS against the resolution is shown in Fig. 16 for Taylor–Green vortices at Re = 1000. The computing expense increases as $1/dx$ increases, approximately as a power law with an exponent of 2.5.

All the four methods could manage to simulate the flow development with a low Reynolds number, $Re = 10$. ISPH_DF cannot stably simulate higher Reynolds cases. Although ISPH_DI could keep well distributed particle spacings, the numerical noise generated by this method contaminates the results under higher Reynolds number situations. ISPH_DFDI stably and accurately simulates cases with Reynolds numbers, $Re = 10$ and $Re = 100$. But with $Re = 1000$, small numerical noise appears on the profile, shown in Fig. 12. ISPH_DFS efficiently stabilizes all simulations, and supplies predictions with less numerical noise for a given resolution. Fig. 15 shows that ISPH_DFS is only first-order accurate in space, probably caused by the limited interpolation accuracy of SPH [24].

6.2. Vortex spin-down results

In vortex spin-down simulations, cases with $Re = 10, Re = 100$ and $Re = 1000$ are simulated. Finite volume simulations, with STAR_CD commercial software, were run as comparison against projection-based ISPH methods. The mesh convergence test with uniform meshes, from 40×40, 80×80, to 160×160, is conducted in finite volume simulations. Converged results are obtained with a resolution of 160×160 and are used for the comparison. With $Re = 10$, all four methods manage to provide accurate predictions, shown in Fig. 17. However, when the Reynolds number increases to 100, the simulation became unstable with ISPH_DF. As with the Taylor–Green vortex simulations, particle spacings are strongly distorted, which makes simulations quite unstable.

Figs. 17 and 20 present the simulation results with $Re = 10$ situation using all four ISPH methods. All the methods provide very good prediction for the velocity and kinetic energy decay. Note that for ISPH_DFDI pressure is used as an internal mechanism to drive velocity. Since this is applied in the correction at the second half time step, Eq. (32), the computed pressure appears as twice the actual pressure. For $Re = 100$ or higher, ISPH_DF does not provide stable simulations, as explained before. With ISPH_DI, the simulation is stabilized. However, this method could not predict the fluid field accurately. Much numerical noise appears in the simulations, shown in Figs. 19, 21 and 22. ISPH_DFDI and ISPH_DFS both accurately predict the flow development under the situation of $Re = 100$, presented in Figs. 18 and 21. For $Re = 1000$, they both underpredict the kinetic energy decaying rate although the velocity field is well prescribed at a physical time of 1 s, shown in Figs. 19 and 22. With $Re = 1000$, ISPH_DFDI produces small numerical noise at the beginning of flow development, shown in the enlarged part in Fig. 22.

In Table 2, the computing costs of all the four methods are listed. Increasing Reynolds number from 10 to 1000, the computing expense increases markedly with ISPH_DFDI. For higher Reynolds numbers, the internal iteration in ISPH_DFDI, Eq. (30), sometimes needs more than 10 cycles to regularize particle spacing. It can be seen that ISPH_DFS is only slightly more computationally expensive than ISPH_DF and ISPH_DI, while providing good stability and accuracy.
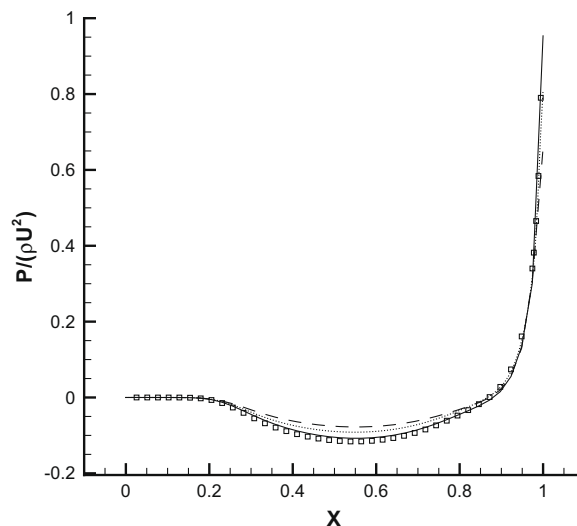

Fig. 28. Pressure profile along the square diagonal, from (0.0,0.0) to (1.0,1.0), in lid-driven cavity, $Re = 1000$. □ = STAR-CD with 160×160 resolution; --- = ISPH_DFS with 81×81 resolution; ⋯ = ISPH_DFS with 161×161 resolution; — = ISPH_DFS with 241×241 resolution.

6.3. Lid-driven cavity results

As a widely-studied test case, the lid-driven cavity is used to further validate the ISPH_DFS algorithm. Reynolds numbers, $Re = 100, Re = 400$, and $Re = 1000$, are simulated and results are compared with data from [10]. Convergence tests for ISPH_DFS, with different resolutions are conducted for all Reynolds numbers.

In Figs. 23–25, the velocity profiles in the middle of the domain, $x = 0.5\ m$ and $y = 0.5\ m$, are presented for each Reynolds number, $Re = 100, Re = 400, Re = 1000$, respectively. With increasing the resolution, the simulation results are converging to Ghia's results [10]. However, as the Reynolds number increases, resolution has to also increase to produce satisfactory results.

Figs. 26–28 present pressure profiles along the diagonal line, from $(0.0\ m, 0.0\ m)$ to $(1.0\ m, 1.0\ m)$. With a resolution of 160×160, STAR-CD can achieve almost the same accuracy for velocity as [10], and corresponding pressure results are used for validation. ISPH_DFS produces almost identical results for $Re = 100$ for all resolutions. For the higher Reynolds numbers, results can be seen to converge with increasing resolution, with a close agreement with 240×240 resolution.

With the same resolution, ISPH_DFS predicts flows less accurately than the finite volume method, which is probably caused by the first-order accuracy limitation of ISPH_DFS.

7. Conclusion

The accuracy and stability of three existing projection-based incompressible SPH (ISPH) methods are tested for Taylor–Green and vortex spin-down flows. A new projection-based ISPH method is introduced which maintains stability and accuracy without loss of efficiency. It can be concluded that:

(1) ISPH_DF provides accurate predictions in certain cases. However, when particle spacing becomes highly distorted, errors caused by anisotropic particle spacings accumulate. ISPH_DF exhibits instability in such cases.
(2) ISPH_DI overcomes the instability introduced by ill-distributed particles. However, it is shown that this method does not give accurate predictions for these flows. The numerical noise can be extremely high.
(3) By combining the accuracy characteristics of ISPH_DF and the stability of ISPH_DI, ISPH_DFDI produces accurate and stable simulations, with evenly distributed particles. However, efficiency is sacrificed, with the method often requiring many internal iterations. Also it can be observed in Figs. 12 and 22 that, with the same numerical parameters, ISPH_DFDI could introduce small numerical noise in the result.
(4) Based on ISPH_DF, ISPH_DFS provides a stable algorithm without sacrificing efficiency. Particles are shifted slightly across streamlines, avoiding particle spacing distortion and the error resulting from particle clustering, and their hydrodynamic properties are adjusted by Taylor series interpolation. This projection-based ISPH method has the first-order spatial accuracy, compared with the second order for finite volume methods, producing slower convergence. Similar results were obtained by redistributing particles on a uniform grid [3], tested for Taylor–Green vortices, but the attraction of a mesh-free method is partially lost.

Acknowledgments

References

[1] J. Bonet, T.-S.L. Lok, Variational and momentum preservation aspects of smooth particle hydrodynamics formulations, Comput. Meth. Appl. Mech. Eng. 180 (1999) 97–115.
[2] S. Bǿrve, M. Omang, J. Trulsen, Regularized smoothed particle hydrodynamics with improved multi-resolution handling, J. Comput. Phys. 208 (2005) 345–367.
[3] A.K. Chaniotis, D. Poulikakos, P. Koumoutsakos, Remeshed smoothed particle hydrodynamics for the simulation of viscous and heat conducting flows, J. Comput. Phys. 182 (2002) 67–90.
[4] A.J. Chorin, Numerical solution of the Navier–Stokes equations, J. Math. Comp. 22 (1968) 745–762.
[5] F. Colin, R. Egli, F.Y. Lin, Computing a null divergence velocity field using smoothed particle hydrodynamics, J. Comput. Phys. 217 (2006) 680–692.
[6] S.J. Cummins, M. Rudman, An SPH projection method, J. Comput. Phys. 152 (1999) 584–607.
[7] R.A. Dalrymple, B.D. Rogers, Numerical modeling of water waves with the SPH method, Coastal Eng. 53 (2006) 141–147.
[8] M. Ellero, M. Serrano, P. Español, Incompressible smoothed particle hydrodynamics, J. Comput. Phys. 226 (2007) 1731–1752.
[9] J. Fang, A. Parriaux, A regularized Lagrangian finite point method for the simulation of incompressible viscous flows, J. Comput. Phys. 227 (2008) 8894–8908.
[10] U. Ghia, K.N. Ghia, C.T. Shin, High-Re solutions for incompressible flow using the Navier–Stokes equations and multigrid method, J. Comput. Phys. 48 (1982) 387–411.
[11] R.A. Gingold, J.J. Monaghan, Smoothed particle hydrodynamics -theory and application to non-spherical stars, Mon. Not. R. Astron. Soc. 181 (1977) 375–389.
[12] X.Y. Hu, N.A. Adams, An incompressible multi-phase SPH method, J. Comput. Phys. 227 (2007) 264–278.

[13] H. Jasak, A. Gosman, Automatic resolution control for the finite-volume method. Part 1: A-posteriori error estimates, Numer. Heat Transfer, Part B: Fundamentals 38 (2000) 237–256.
[14] S. Koshizuka, H. Tamako, Y. Oka, A particle method for incompressible viscous flow with fluid fragmentation, J. Comput. Fluid Dyn. 4 (1995) 29–46.
[15] S. Koshizuka, A. Nobe, Y. Oka, Numerical analysis of breaking waves using the moving particle semi-implicit method, Int. J. Numer. Meth. Fluids 26 (1998) 751–769.
[16] E.-S. Lee, Truly incompressible approach for computing incompressible flow in SPH and comparisons with the traditional weakly compressible approach, Ph.D. Thesis, University of Manchester, Manchester, UK, 2007.
[17] E.-S. Lee, C. Moulinec, R. Xu, D. Violeau, D. Laurence, P. Stansby, Comparisons of weakly compressible and truly incompressible algorithms for the SPH mesh free particle method, J. Comput. Phys. 227 (2008) 8417–8436.
[18] L.B. Lucy, Numerical approach to the testing of the fission hypothesis, Astron. J. 82 (1977) 1013–1024.
[19] J.J. Monaghan, SPH without a tensile instability, J. Comput. Phys. 159 (2000) 290–311.
[20] J.J. Monaghan, Smoothed particle hydrodynamics, Rep. Prog. Phys. 68 (2005) 1703–1759.
[21] J.P. Morris, P.J. Fox, Y. Zhu, Modeling low Reynolds number incompressible flows using SPH, J. Comput. Phys. 136 (1997) 214–226.
[22] R. Nestor, M. Basa and N. Quinlan, Moving boundary problems in the finite volume particle method, in: ERCOFTAC SIG SPHERIC IIIrd International workshop, Lausanne, Switzland, 2008, pp. 109–114.
[23] G. Oger, M. Doring, B. Alessandrini, P. Ferrant, An improved SPH method: towards higher order convergence, J. Comput. Phys. 225 (2007) 1472–1492.
[24] H.F. Schwaiger, An implicit corrected SPH formulation for thermal diffusion with linear free surface boundary conditions, Int. J. Numer. Meth. Eng. 75 (2008) 647–671.
[25] S. Shao, E.Y.M. Lo, Incompressible SPH method for simulating Newtonian and non-Newtonian flows with a free surface, Adv. Water Resour. 26 (2003) 787–800.
[26] SPHysics, open-source SPH free-surface flow solver, SPHysics URL: http://wiki.manchester.ac.uk/sphysics/index.php/Main_Page. First posting 01 August 2007, last visited 29 February 2009.